

---

# Synthetic red supergiant explosion model grid for systematic characterization of Type II supernovae

Takashi J. MORIYA<sup>1,2</sup>, Bhagya M. SUBRAYAN,<sup>3</sup> Dan MILISAVLJEVIC<sup>3,4</sup> and Sergei I. BLINNIKOV<sup>5,6</sup>

<sup>1</sup>National Astronomical Observatory of Japan, National Institutes of Natural Sciences, 2-21-1 Osawa, Mitaka, Tokyo 181-8588, Japan

<sup>2</sup>School of Physics and Astronomy, Faculty of Science, Monash University, Clayton, Victoria 3800, Australia

<sup>3</sup>Department of Physics and Astronomy, Purdue University, 525 Northwestern Ave, West Lafayette, IN 47907, USA

<sup>4</sup>Integrative Data Science Initiative, Purdue University, West Lafayette, IN 47907, USA

<sup>5</sup>NRC Kurchatov Institute, 123182 Moscow, Russia

<sup>6</sup>Dukhov Automatics Research Institute (VNIIA), 127055 Moscow, Russia

\*E-mail: takashi.moriya@nao.ac.jp

Received 2023 March 6; Accepted 2023 March 6

## Abstract

A new model grid containing 228,016 synthetic red supergiant explosions (Type II supernovae) is introduced. Time evolution of spectral energy distributions from 1 Å to 50,000 Å (100 frequency bins in a log scale) is computed at each time step up to 500 days after explosion in each model. We provide light curves for the filters of the Vera C. Rubin Observatory's Legacy Survey of Space and Time (LSST), Zwicky Transient Facility (ZTF), Sloan Digital Sky Survey (SDSS), and the Neil Gehrels Swift Observatory, but light curves for any photometric filters can be constructed by convolving any filter response functions to the synthetic spectral energy distributions. We also provide bolometric light curves and photosphere information such as photospheric velocity evolution. The parameter space covered by the model grid is five progenitor masses (10, 12, 14, 16, and 18  $M_{\odot}$  at the zero-age main sequence, solar metallicity), ten explosion energies (0.5, 1.0, 1.5, 2.0, 2.5, 3.0, 3.5, 4.0, 4.5, and  $5.0 \times 10^{51}$  erg), nine  $^{56}\text{Ni}$  masses (0.001, 0.01, 0.02, 0.04, 0.06, 0.08, 0.1, 0.2, and 0.3  $M_{\odot}$ ), nine mass-loss rates ( $10^{-5.0}$ ,  $10^{-4.5}$ ,  $10^{-4.0}$ ,  $10^{-3.5}$ ,  $10^{-3.0}$ ,  $10^{-2.5}$ ,  $10^{-2.0}$ ,  $10^{-1.5}$ , and  $10^{-1.0}$   $M_{\odot} \text{ yr}^{-1}$  with a wind velocity of 10  $\text{km s}^{-1}$ ), six circumstellar matter radii (1, 2, 4, 6, 8, and  $10 \times 10^{14}$  cm), and ten circumstellar structures ( $\beta = 0.5, 1.0, 1.5, 2.0, 2.5, 3.0, 3.5, 4.0, 4.5,$  and 5.0).  $^{56}\text{Ni}$  is assumed to be uniformly mixed up to the half mass of a hydrogen-rich envelope. This model grid can be a base for rapid characterizations of Type II supernovae with sparse photometric sampling expected in LSST through a Bayesian approach, for example. The model grid is available at <https://doi.org/10.5061/dryad.pnvx0k6sj>.

**Key words:** supernova: general – stars: massive – supergiants – stars: winds, outflows

---

## 1 Introduction

The number of supernova (SN) discovery has increased dramatically in the last decade thanks to many large-scale optical transient surveys (e.g., Nicholl 2021). The increase of SN discovery led to discoveries of rare SNe such as superluminous SNe (e.g., Quimby et al. 2011) and ultra-stripped SNe (e.g., De et al. 2018). At the same time, the number of commonly observed SNe has also increased explosively. For example, hundreds of Type II SNe have been reported in a year in the last few years<sup>1</sup>. We may even have  $10^5$  Type II SNe per year in the coming era of the Vera C. Rubin Observatory's LSST (LSST Science Collaboration et al. 2009), although the LSST survey strategy has not been fixed yet.

Having a large number of SNe allows us to study their statistical properties. Especially, statistical studies of Type II SNe provide us the standard nature of core-collapse SN explosions because they are the most common explosions of massive stars (Li et al. 2011; Shivvers et al. 2017; Perley et al. 2020). Light-curve modeling of a large number of Type II SNe has been used to estimate the general properties of Type II SNe such as their progenitor mass, explosion energy, and  $^{56}\text{Ni}$  mass (e.g., Utrobin & Chugai 2013; Nagy et al. 2014; Pumo et al. 2017; Morozova et al. 2018; Martinez et al. 2022b). The estimated properties have been compared to predictions from SN explosion simulations so that the standard SN explosion mechanism can be revealed (e.g., Ugliano et al. 2012; Nakamura et al. 2015; Müller et al. 2016; Sukhbold et al. 2016; Burrows & Vartanyan 2021). Having a large number of Type II SNe will also be beneficial for the use of Type II SNe as a distance indicator (e.g., de Jaeger et al. 2020; de Jaeger et al. 2017; Gall et al. 2018; Nadyozhin 2003; Hamuy & Pinto 2002).

The systematic light-curve modeling of a large number of Type II SNe has been mostly performed by using bolometric light curves because of the difficulty in modeling multi-frequency light curves. Usually, bolometric light curves are constructed from observations, and then they are compared with theoretical models for parameter estimations (e.g., Martinez et al. 2022a; Martinez et al. 2022b; Martinez et al. 2022c). However, this kind of studies are only possible for well-observed Type II SNe with which bolometric light curves can be estimated. Unfortunately, ongoing large-scale transient surveys such as ZTF (Bellm et al. 2019) have only a few bands to cover a wide field frequently, and it is difficult to construct bolometric light curves based only on photometry data provided by ZTF. The LSST survey may also not provide densely sampled

photometric data covering a wide wavelength range required to estimate bolometric luminosity. In order to make full use of a large number of Type II SNe discovered by ZTF, LSST, and other large-scale transient surveys, it is ideal to make a direct comparison between theoretical models and observations in observed bands without constructing bolometric light curves.

Light-curve modeling of Type II SNe in multi-frequencies has been performed, but they are limited to well-observed Type II SNe (e.g., Baklanov et al. 2005; Tominaga et al. 2009; Hillier & Dessart 2019; Kozyreva et al. 2022a). Multi-frequency light-curve modeling takes time and it has been difficult to perform such modeling systematically for a large number of Type II SNe. However, Förster et al. (2018) demonstrated that a systematic Bayesian parameter estimation for a large number of Type II SNe with two-band observations is feasible. They adopted a large grid of pre-computed multi-frequency light-curve models by Moriya et al. (2018), and used it to estimate the properties of circumstellar matter (CSM) around Type II SNe. A drawback of this approach is that pre-computed multi-frequency light-curve models need to cover a wide parameter range. Because Förster et al. (2018) focused on the rising part of Type II SNe, the adopted models had a fixed amount of  $^{56}\text{Ni}$  that does not affect early light curves of Type II SNe. Still, hundreds of pre-computed models were required for the Bayesian parameter estimation to reveal that most Type II SNe are affected by CSM interaction in early phases (see also Morozova et al. 2017).

In this paper, we introduce a new synthetic model grid of Type II SNe. The new model grid contains 228,016 Type II SN models with different combinations of progenitor mass, explosion energy,  $^{56}\text{Ni}$  mass, mass-loss rate, CSM radius, and CSM structure in much wider parameter ranges than the previous model grid of Moriya et al. (2018). We provide time evolution of spectral energy distributions (SEDs) from  $1 \text{ \AA}$  to  $50,000 \text{ \AA}$  at each time step for all the models. Thus, our model grid can be used to estimate light-curve evolution at any given photometric bands. Any extinction can also be directly applied to synthetic SEDs. In addition, our synthetic SEDs can be shifted at any redshifts so that the  $K$  correction can be properly taken into account (see Tominaga et al. 2011 for an example). We also provide photosphere information for all the models that is often required to break the degeneracy in estimating SN properties. A subset of this new model grid has already been successfully used to estimate the properties of 45 Type II SNe discovered by ZTF (Subrayan et al. 2022).

The rest of this paper is organized as follows. We

<sup>1</sup><https://www.wis-tns.org/>

**Table 1.** Progenitor properties.

ZAMS Mass	Final Mass	H-rich envelope mass	Radius
10 $M_{\odot}$	9.7 $M_{\odot}$	7.2 $M_{\odot}$	510 $R_{\odot}$
12 $M_{\odot}$	10.9 $M_{\odot}$	7.8 $M_{\odot}$	640 $R_{\odot}$
14 $M_{\odot}$	12.1 $M_{\odot}$	8.1 $M_{\odot}$	790 $R_{\odot}$
16 $M_{\odot}$	13.1 $M_{\odot}$	8.4 $M_{\odot}$	890 $R_{\odot}$
18 $M_{\odot}$	14.9 $M_{\odot}$	9.5 $M_{\odot}$	970 $R_{\odot}$

present our model setups and numerical method used for our numerical calculations in Section 2. We discuss some representative properties of our Type II SN models in Section 3. We provide a brief summary of this paper in Section 4.

## 2 Model setups

### 2.1 Initial conditions

We adopt red supergiant (RSG) Type II SN progenitors in Sukhbold et al. (2016). We take progenitors with the zero-age main sequence (ZAMS) masses of 10, 12, 14, 16, and 18  $M_{\odot}$ , which is in the estimated mass range of Type II SN progenitors (e.g., Smartt 2015; Davies & Beasor 2018; Davies & Beasor 2020; Kochanek 2020; Rodríguez 2022). They have solar metallicity at ZAMS. The progenitor properties are summarized in Table 1. We assume a mass cut of 1.4  $M_{\odot}$ , and put the structure above the mass cut in our explosion calculations. The density structure of the progenitor models is presented in Fig. 1.

We attach confined CSM on top of the progenitors. It has been recently recognized that confined dense CSM often exists around Type II SN progenitors at the time of explosion (e.g., Yaron et al. 2017; Bruch et al. 2021; Bruch et al. 2022; Jacobson-Galán et al. 2022), and it strongly affect the early phases of Type II SN properties (e.g., Moriya et al. 2011; Morozova et al. 2018; Haynie & Piro 2021; Kozyreva et al. 2022a; Dessart & Hillier 2022). The origin and structure of the confined CSM are still unknown (e.g., Yoon & Cantiello 2010; Fuller 2017; Dessart et al. 2017; Morozova et al. 2020; Tsuna et al. 2021; Ko et al. 2022). In this work, we adopt the following CSM density structure based on the previous studies by Moriya et al. (2017); Moriya et al. (2018),

$$\rho_{\text{CSM}}(r) = \frac{\dot{M}}{4\pi v_{\text{wind}}(r)} r^{-2}, \quad (1)$$

where  $r$  is the radius,  $\dot{M}$  is the mass-loss rate, and  $v_{\text{wind}}$  is the wind velocity. For the wind velocity, we adopt

$$v_{\text{wind}}(r) = v_0 + (v_{\infty} - v_0) \left(1 - \frac{R_0}{r}\right)^{\beta}, \quad (2)$$

where  $v_0$  is an initial wind velocity at a progenitor surface,  $v_{\infty}$  is a terminal wind velocity,  $R_0$  is a progenitor radius,

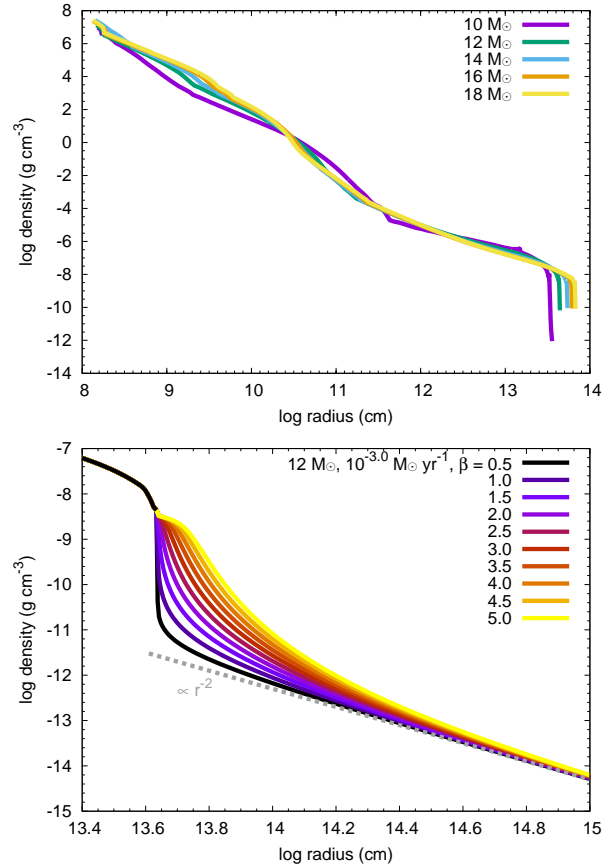


**Fig. 1.** *Top:* Density structure of the progenitor models above a mass cut of 1.4  $M_{\odot}$ . *Bottom:* Examples of CSM density structure with various  $\beta$ .

and  $\beta$  is a wind structure parameter determined by the efficiency of wind acceleration. RSGs are known to have slow wind acceleration with  $\beta > 1$  (e.g., Schroeder 1985; Baade et al. 1996). This expression assumes that confined CSM around Type II SN progenitors is caused by strong stellar wind. Although it is still not clear if such a strong wind model is responsible for the formation of confined CSM around Type II SNe (Davies et al. 2022), it provides a good explanation for early photometric properties of Type II SNe (Förster et al. 2018). We choose  $v_0$  so that CSM structure is smoothly connected at the progenitor surface.  $v_{\infty}$  is set to 10  $\text{km s}^{-1}$ , which is a typical wind velocity of RSGs (e.g., Maun & Josselin 2011; Goldman et al. 2017). In our model grid, we change  $\dot{M}$  and  $\beta$ . We adopt  $\dot{M} = 10^{-5.0}, 10^{-4.5}, 10^{-4.0}, 10^{-3.5}, 10^{-3.0}, 10^{-2.5}, 10^{-2.0}, 10^{-1.5}$ , and  $10^{-1.0} M_{\odot} \text{ yr}^{-1}$  and  $\beta = 0.5, 1.0, 1.5, 2.0, 2.5, 3.0, 3.5, 4.0, 4.5$ , and 5.0. The radius of the confined CSM is constrained to be less than around  $10^{15}$  cm (Yaron et al. 2017). Thus, we adopt the CSM radius of  $10^{14}, 2 \times 10^{14}, 4 \times 10^{14}, 6 \times 10^{14}, 8 \times 10^{14}$ , and  $10^{15}$  cm. Figure 1 presents some examples of CSM

**Table 2.** Parameters in the model grid.

ZAMS Mass ( $M_{\odot}$ )	10, 12, 14, 16, 18
$\dot{M}$ ( $M_{\odot} \text{ yr}^{-1}$ )	$10^{-5.0}, 10^{-4.5}, 10^{-4.0}, 10^{-3.5}, 10^{-3.0}, 10^{-2.5}, 10^{-2.0}, 10^{-1.5}, 10^{-1.0}$
$\beta$	0.5, 1.0, 1.5, 2.0, 2.5, 3.0, 3.5, 4.0, 4.5, 5.0
CSM radius ( $10^{14}$ cm)	1, 2, 4, 6, 8, 10
Explosion energy (B)	0.5, 1.0, 1.5, 2.0, 2.5, 3.0, 3.5, 4.0, 4.5, 5.0
$^{56}\text{Ni}$ mass ( $M_{\odot}$ )	0.001, 0.01, 0.02, 0.04, 0.06, 0.08, 0.1, 0.2, 0.3

density structure with various  $\beta$ . The CSM abundance is set to be the same as that at the progenitor surface.

## 2.2 Explosion properties

We adopt explosion energies of 0.5, 1.0, 1.5, 2.0, 2.5, 3.0, 3.5, 4.0, 4.5, and 5.0 B where  $1 \text{ B} \equiv 10^{51} \text{ erg}$ . While explosion energy of Type II SNe is typically estimated to be 0.1 – 1.5 B (e.g., Martinez et al. 2022c), we extend our models to higher explosion energy because magnitude limited transient surveys tend to discover SNe with large luminosity having high explosion energy.

The mass of  $^{56}\text{Ni}$  strongly affects light-curve properties of Type II SNe at late phases. In our model grid, we adopt  $^{56}\text{Ni}$  mass of 0.001, 0.01, 0.02, 0.04, 0.06, 0.08, 0.1, 0.2, and 0.3  $M_{\odot}$ , which is in the range of  $^{56}\text{Ni}$  mass estimated from observations (e.g., Anderson 2019). One important property that is related to  $^{56}\text{Ni}$  and determines Type II light-curve features is the degree of  $^{56}\text{Ni}$  mixing (e.g., Kasen & Woosley 2009; Bersten et al. 2011; Dessart et al. 2013; Moriya et al. 2016). Although it is likely that  $^{56}\text{Ni}$  is mixed to hydrogen-rich envelopes in Type II SNe (e.g., Singh et al. 2019), it is not exactly clear how far in the hydrogen-rich envelopes  $^{56}\text{Ni}$  is mixed. In our model grid, we assume that  $^{56}\text{Ni}$  is uniformly mixed up to the half mass of the hydrogen-rich envelope so that an average effect of  $^{56}\text{Ni}$  mixing is taken into account.

We have introduced all the parameters in our model grid that is summarized in Table 2. If we take all the parameter combinations, we should have 243,000 models in total in our model grid. However, computations of some models failed for various numerical reasons. Failed models are not concentrated on particular parameter ranges. We succeeded in completing the numerical calculations for 228,016 models which are 94% of the total parameter combination. We introduce our numerical methods in the next section.

## 2.3 Numerical computations

We adopt the one-dimensional multi-frequency radiation hydrodynamics code STELLA to construct the model grid

(Blinnikov et al. 1998; Blinnikov et al. 2000; Blinnikov et al. 2006). STELLA has been used for Type II SN light-curve modeling intensively (e.g., Goldberg et al. 2019; Hiramatsu et al. 2021; Kozyreva et al. 2022b for recent examples). STELLA provides synthetic light curves that are consistent with other radiation transport codes used in SN modeling (Blondin et al. 2022). Being a radiation hydrodynamics code, STELLA can take the interaction between SN ejecta and CSM into account in computing light curves. We introduce STELLA briefly.

STELLA evaluates the evolution of hydrodynamic and radiation parameters in each time step by using the variable Eddington factor method. Explosions are initiated by injecting thermal energy required to achieve each explosion energy above the mass cut at 1.4  $M_{\odot}$  in the first 0.1 sec. Radiation is treated in multi-frequency, and STELLA provides a SED at each time step. We adopt the standard 100 frequency bins from 1 Å to 50,000 Å in a log scale. Opacity in each frequency bin is estimated based on the atomic levels from the Saha equation by assuming the local thermodynamic equilibrium. Bremsstrahlung, bound-free transitions, bound-bound transitions, photoionization, and electron scattering are taken into account in opacity. Gas temperature and radiation temperature are treated separately. We define photosphere as a location where a Rosseland-mean optical depth becomes 2/3. We record radius, velocity, mass coordinate, and temperature at the photosphere.

Bolometric light curves are computed by integrating SEDs at each time step. Light curves in any photometric bands can be obtained by convolving SEDs with filter response functions. We provide light curves for the  $u$ ,  $g$ ,  $r$ ,  $i$ ,  $z$ , and  $y$  filters of LSST<sup>2</sup>, the  $g$ ,  $r$ , and  $i$  filters of ZTF (Bellm et al. 2019), the  $g$ ,  $r$ , and  $i$  filters of SDSS (Doi et al. 2010), and the  $UVW2$ ,  $UVM2$ ,  $UVW1$ ,  $U$ ,  $B$ , and  $V$  filters of the Neil Gehrels Swift Observatory (Poole et al. 2008; Breeveld et al. 2011) at the rest frame in the absolute AB magnitude. The absolute AB magnitude at a  $x$  filter is evaluated by

$$M_{\text{AB},x} = -2.5 \log \frac{\int F_{\nu}(\nu) S_x(\nu) d\nu / \nu}{\int S_x(\nu) d\nu / \nu} - 48.60, \quad (3)$$

<sup>2</sup> <https://github.com/lstst/throughputs/tree/main/baseline>

where  $\nu$  is the frequency,  $F_\nu(\nu)$  is the absolute synthetic flux observed at 10 pc in  $\text{erg s}^{-1} \text{cm}^{-2} \text{Hz}^{-1}$ , and  $S_x(\nu)$  is a filter response function (e.g., Bessell & Murphy 2012).

### 3 Some light-curve properties

The model grid computed by the method discussed so far is available at <https://doi.org/10.5061/dryad.pnvx0k6sj>. We present some features of Type II SNe predicted by the model grid in this section.

Figure 2 shows examples of our model grid data. Light curves and photospheric velocity from two different mass-loss rates ( $10^{-5.0}$  and  $10^{-3.0} M_\odot \text{yr}^{-1}$ ) are presented. We can see clearly the effects of dense confined CSM in early phases in these examples. The early bolometric luminosity becomes higher when the mass-loss rate is higher because of extra radiation from CSM interaction. The rise time in bolometric light curves increases with higher mass-loss rates due to increased diffusion time in CSM. The rise times in the optical bands become shorter with higher mass-loss rates because contributions of the luminosity from CSM interaction becomes dominant in optical in early phases. We can find that photospheric velocity is also strongly affected by the CSM interaction in early phases while the CSM interaction continues. The photosphere can be located within CSM in early phases and the photospheric velocity can be low at the beginning. We can observe the effect of acceleration of CSM by radiation in the photospheric velocity before the shock passes through the CSM (cf. Tsuna et al. 2023).

Figure 3 illustrates how each parameter affects light-curve properties in the LSST  $g$  band. The rise times of Type II SNe are mostly affected by CSM properties and explosion energy. The tail phase is mostly affected by  $^{56}\text{Ni}$  mass, although explosion energy can also change the light-curve decline rate in the tail phase. The plateau magnitude and duration are affected by progenitor mass, explosion energy, and  $^{56}\text{Ni}$  mass. Mass-loss rates also affect the plateau properties when they are high enough.

The short rise times observed in Type II SNe (e.g., González-Gaitán et al. 2015; Gall et al. 2015) have been related to the existence of dense confined CSM around Type II SN progenitors (e.g., Förster et al. 2018). We discuss how the rise time and peak luminosity in Type II SNe are affected by confined CSM. Figures 4 and 5 present how mass-loss rates affect the rise time and peak luminosity distributions in the LSST  $g$  and  $r$  band, respectively, for the case of the  $12 M_\odot$  progenitor. The  $g$  band rise time is around 20 days when the mass-loss rate is small. The peak magnitude gap at around  $-16.5$  mag is caused by the lack of models between 0.5 B and 1.0 B, i.e., most

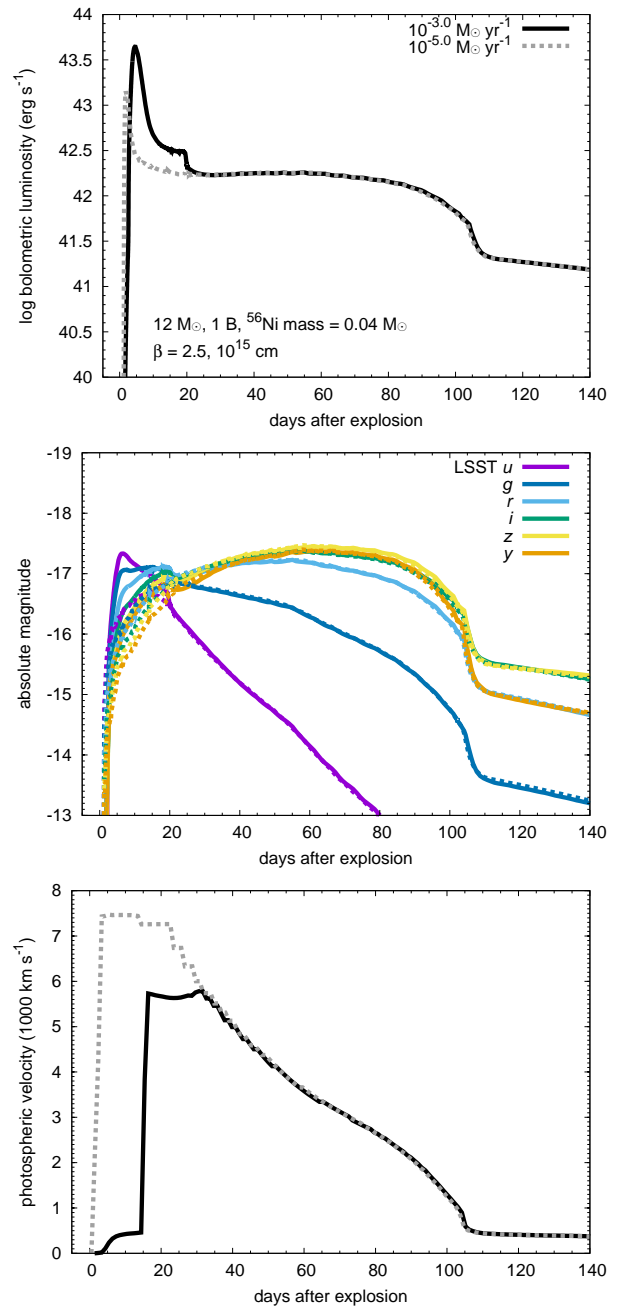


**Fig. 2.** Examples of light curves and photospheric velocities with low ( $10^{-5.0} M_\odot \text{yr}^{-1}$ , dashed lines) and high ( $10^{-3.0} M_\odot \text{yr}^{-1}$ , solid lines) mass-loss rates in the model grid. The two models have the same progenitor ( $12 M_\odot$ ), explosion energy (1 B),  $^{56}\text{Ni}$  mass ( $0.04 M_\odot$ ),  $\beta$  (2.5), and CSM radius ( $10^{15} \text{cm}$ ). The top panel presents bolometric light curves, the middle panel shows optical light curves in the LSST filters, and the bottom panel shows photospheric velocities.

0.5 B explosion models have peak magnitudes fainter than  $-16.5$  mag while most models about 1.0 B have peak magnitudes brighter than  $-16.5$  mag. We start to find a population of Type II SNe with short rise times of around 5 days when  $\dot{M} \gtrsim 10^{-3.0} M_{\odot} \text{ yr}^{-1}$ . As the mass-loss rate increases, the diffusion time in CSM becomes longer and thus the rise time becomes longer again at  $\dot{M} \gtrsim 10^{-1.5} M_{\odot} \text{ yr}^{-1}$ . The  $r$  band rise time is less sensitive to mass-loss rates, but we start to see the similar effects in the  $r$  band rise time when  $\dot{M} \gtrsim 10^{-2.5} M_{\odot} \text{ yr}^{-1}$ .

When  $\dot{M} \gtrsim 10^{-3.0} M_{\odot} \text{ yr}^{-1}$ , we can still find some populations of Type II SNe with long rise times as in the lower  $\dot{M}$  models in Fig. 4. This is because of the existence of CSM with small radii. Figure 6 shows how the CSM radius affects the rise time and peak luminosity in the LSST  $g$  band for a fixed mass-loss rate of  $10^{-2.5} M_{\odot} \text{ yr}^{-1}$ . Even if the mass-loss rate is high, a population of short rise times remain if a CSM radius is small ( $\lesssim 2 \times 10^{14}$  cm). The population of Type II SNe with short rise times start to appear when the CSM radius is more than  $4 \times 10^{14}$  cm.

Fig. 7 demonstrates how the CSM mass ( $M_{\text{CSM}}$ ) affects the rise time and peak luminosity distributions in the LSST  $g$  band. The population of Type II SNe with short rise times can be found when  $M_{\text{CSM}} \gtrsim 0.1 M_{\odot}$ . When the CSM mass exceeds about  $1 M_{\odot}$ , the rise time becomes long because of large diffusion time in CSM.

We focused on the  $12 M_{\odot}$  progenitor models so far. Figure 8 summarizes the rise time and peak luminosity distributions from the other progenitors in the LSST  $g$  band. While the rise time and peak luminosity distributions are affected by the differences in the progenitors when the mass-loss rate is low, their dependence on the progenitors becomes less significant as the mass-loss rate becomes higher. This is because they start to be mainly affected by the CSM properties.

Properties of photosphere are provided in the model grid, and they also give important and interesting insight to Type II SNe. As an example, we present a relation between photospheric velocity and the LSST  $g$  band magnitude at 50 days after explosion in the  $12 M_{\odot}$  progenitor in Fig. 9. Overall, we can see a trend that explosions with higher explosion energy have higher photospheric velocities and higher luminosities. The relation between photospheric velocity and  $g$  band magnitude is strongly affected by CSM properties as well. We can find that a population of Type II SNe with high luminosity is caused by the models with large mass-loss rates exceeding  $10^{-2.0} M_{\odot} \text{ yr}^{-1}$ . This bright population appears even if explosion energy and photospheric velocity are small regardless of the progenitor mass (Fig. 10). Such a population is starting to be identified observationally (Rodríguez et al. 2020), and

it also demonstrates the importance of the role of CSM in understanding the diversity in Type II SNe.

## 4 Summary

We have introduced a new model grid of Type II SNe containing 228,016 synthetic explosion models. Parameters that changed are progenitor mass, explosion energy,  $^{56}\text{Ni}$  mass, mass-loss rate, CSM density structure and CSM radius. For each model, we provide SED ( $1 - 50,000 \text{ \AA}$ ), absolute magnitudes in the LSST, ZTF, SDSS, and Swift filters in each time step. Photosphere information is also provided. Light curves in any photometric bands can be constructed by using SEDs. Our model grid confirms the importance of confined CSM in shaping the diversities observed in Type II SNe. The model grid is available at <https://doi.org/10.5061/dryad.pnvx0k6sj>.

In the upcoming era of LSST, rapid characterization of Type II SNe with limited photometry information will be required. Thus, our synthetic model grid of Type II SNe that allows direct comparison of observations and models is expected to be important. The new model grid can be a base for a Bayesian parameter estimation of Type II SNe that has already been demonstrated to be powerful (Subrayan et al. 2022).

This model set can also be used to search for predicted properties of Type II SNe. For example, bright Type II SNe with low photospheric velocity are predicted to be mostly caused by Type II SNe with high mass-loss rates exceeding  $10^{-2.0} M_{\odot} \text{ yr}^{-1}$  (Fig. 9). More investigation into the model grid properties would also help us understand the origin of diversity in Type II SNe.

## Acknowledgments

Numerical computations were carried out on PC cluster at Center for Computational Astrophysics (CfCA), National Astronomical Observatory of Japan. TJM is supported by the Grants-in-Aid for Scientific Research of the Japan Society for the Promotion of Science (JP20H00174, JP21K13966, JP21H04997). SIB is supported by RSCF grant 19-12-00229 in his work on SN simulations. This research was partly supported by the Munich Institute for Astro-, Particle and BioPhysics (MIAPbP) which is funded by the Deutsche Forschungsgemeinschaft (DFG, German Research Foundation) under Germany's Excellence Strategy – EXC-2094 – 390783311. This research has made use of the Spanish Virtual Observatory (<https://svo.cab.inta-csic.es>) project funded by MCIN/AEI/10.13039/501100011033/ through grant PID2020-112949GB-I00 (Rodrigo et al. 2012; Rodrigo & Solano 2020).

## References

- Anderson, J. P. 2019, *A&A*, 628, A7
- Baade, R., Kirsch, T., Reimers, D., et al. 1996, *ApJ*, 466, 979
- Baklanov, P. V., Blinnikov, S. I., & Pavlyuk, N. N. 2005, *Astronomy Letters*, 31, 429
- Bellm, E. C., Kulkarni, S. R., Barlow, T., et al. 2019, *PASP*, 131, 068003
- Bersten, M. C., Benvenuto, O., & Hamuy, M. 2011, *ApJ*, 729, 61
- Bessell, M., & Murphy, S. 2012, *PASP*, 124, 140
- Blinnikov, S., Lundqvist, P., Bartunov, O., Nomoto, K., & Iwamoto, K. 2000, *ApJ*, 532, 1132
- Blinnikov, S. I., Eastman, R., Bartunov, O. S., Popolitov, V. A., & Woosley, S. E. 1998, *ApJ*, 496, 454
- Blinnikov, S. I., Röpke, F. K., Sorokina, E. I., et al. 2006, *A&A*, 453, 229
- Blondin, S., Blinnikov, S., Callan, F. P., et al. 2022, *A&A*, 668, A163
- Breeveld, A. A., Landsman, W., Holland, S. T., et al. 2011, in *American Institute of Physics Conference Series*, Vol. 1358, *Gamma Ray Bursts 2010*, ed. J. E. McEnery, J. L. Racusin, & N. Gehrels, 373–376
- Bruch, R. J., Gal-Yam, A., Schulze, S., et al. 2021, *ApJ*, 912, 46
- Bruch, R. J., Gal-Yam, A., Yaron, O., et al. 2022, *arXiv e-prints*, [arXiv:2212.03313](https://arxiv.org/abs/2212.03313)
- Burrows, A., & Vartanyan, D. 2021, *Nature*, 589, 29
- Davies, B., & Beasor, E. R. 2018, *MNRAS*, 474, 2116
- . 2020, *MNRAS*, 496, L142
- Davies, B., Plez, B., & Petrault, M. 2022, *MNRAS*, 517, 1483
- De, K., Kasliwal, M. M., Ofek, E. O., et al. 2018, *Science*, 362, 201
- de Jaeger, T., Galbany, L., Filippenko, A. V., et al. 2017, *MNRAS*, 472, 4233
- de Jaeger, T., Galbany, L., González-Gaitán, S., et al. 2020, *MNRAS*, 495, 4860
- Dessart, L., & Hillier, D. J. 2022, *A&A*, 660, L9
- Dessart, L., Hillier, D. J., & Audit, E. 2017, *A&A*, 605, A83
- Dessart, L., Hillier, D. J., Waldman, R., & Livne, E. 2013, *MNRAS*, 433, 1745
- Doi, M., Tanaka, M., Fukugita, M., et al. 2010, *AJ*, 139, 1628
- Förster, F., Moriya, T. J., Maureira, J. C., et al. 2018, *Nature Astronomy*, 2, 808
- Fuller, J. 2017, *MNRAS*, 470, 1642
- Gall, E. E. E., Polshaw, J., Kotak, R., et al. 2015, *A&A*, 582, A3
- Gall, E. E. E., Kotak, R., Leibundgut, B., et al. 2018, *A&A*, 611, A25
- Goldberg, J. A., Bildsten, L., & Paxton, B. 2019, *ApJ*, 879, 3
- Goldman, S. R., van Loon, J. T., Zijlstra, A. A., et al. 2017, *MNRAS*, 465, 403
- González-Gaitán, S., Tominaga, N., Molina, J., et al. 2015, *MNRAS*, 451, 2212
- Hamuy, M., & Pinto, P. A. 2002, *ApJL*, 566, L63
- Haynie, A., & Piro, A. L. 2021, *ApJ*, 910, 128
- Hillier, D. J., & Dessart, L. 2019, *A&A*, 631, A8
- Hiramatsu, D., Howell, D. A., Moriya, T. J., et al. 2021, *ApJ*, 913, 55
- Jacobson-Galán, W. V., Dessart, L., Jones, D. O., et al. 2022, *ApJ*, 924, 15
- Kasen, D., & Woosley, S. E. 2009, *ApJ*, 703, 2205
- Ko, T., Tsuna, D., Takei, Y., & Shigeyama, T. 2022, *ApJ*, 930, 168
- Kochanek, C. S. 2020, *MNRAS*, 493, 4945
- Kozyreva, A., Janka, H.-T., Kresse, D., Taubenberger, S., & Baklanov, P. 2022a, *MNRAS*, 514, 4173
- Kozyreva, A., Klencki, J., Filippenko, A. V., et al. 2022b, *ApJL*, 934, L31
- Li, W., Leaman, J., Chornock, R., et al. 2011, *MNRAS*, 412, 1441
- LSST Science Collaboration, Abell, P. A., Allison, J., et al. 2009, *arXiv e-prints*, [arXiv:0912.0201](https://arxiv.org/abs/0912.0201)
- Martinez, L., Bersten, M. C., Anderson, J. P., et al. 2022a, *A&A*, 660, A40
- . 2022b, *A&A*, 660, A41
- Martinez, L., Anderson, J. P., Bersten, M. C., et al. 2022c, *A&A*, 660, A42
- Mauron, N., & Josselin, E. 2011, *A&A*, 526, A156
- Moriya, T., Tominaga, N., Blinnikov, S. I., Baklanov, P. V., & Sorokina, E. I. 2011, *MNRAS*, 415, 199
- Moriya, T. J., Förster, F., Yoon, S.-C., Gräfenner, G., & Blinnikov, S. I. 2018, *MNRAS*, 476, 2840
- Moriya, T. J., Pruzhinskaya, M. V., Ergon, M., & Blinnikov, S. I. 2016, *MNRAS*, 455, 423
- Moriya, T. J., Yoon, S.-C., Gräfenner, G., & Blinnikov, S. I. 2017, *MNRAS*, 469, L108
- Morozova, V., Piro, A. L., Fuller, J., & Van Dyk, S. D. 2020, *ApJL*, 891, L32
- Morozova, V., Piro, A. L., & Valenti, S. 2017, *ApJ*, 838, 28
- . 2018, *ApJ*, 858, 15
- Müller, B., Heger, A., Liptai, D., & Cameron, J. B. 2016, *MNRAS*, 460, 742
- Nadyozhin, D. K. 2003, *MNRAS*, 346, 97
- Nagy, A. P., Ordasi, A., Vinkó, J., & Wheeler, J. C. 2014, *A&A*, 571, A77
- Nakamura, K., Takiwaki, T., Kuroda, T., & Kotake, K. 2015, *PASJ*, 67, 107
- Nicholl, M. 2021, *Astronomy and Geophysics*, 62, 5.34
- Perley, D. A., Fremling, C., Sollerman, J., et al. 2020, *ApJ*, 904, 35
- Poole, T. S., Breeveld, A. A., Page, M. J., et al. 2008, *MNRAS*, 383, 627
- Pumo, M. L., Zampieri, L., Spiro, S., et al. 2017, *MNRAS*, 464, 3013
- Quimby, R. M., Kulkarni, S. R., Kasliwal, M. M., et al. 2011, *Nature*, 474, 487
- Rodrigo, C., & Solano, E. 2020, in *XIV.0 Scientific Meeting (virtual) of the Spanish Astronomical Society*, 182
- Rodrigo, C., Solano, E., & Bayo, A. 2012, *SVO Filter Profile Service Version 1.0, IVOA Working Draft 15 October 2012*, [doi:10.5479/ADS/bib/2012ivoa.rept.1015R](https://doi.org/10.5479/ADS/bib/2012ivoa.rept.1015R)
- Rodríguez, Ó. 2022, *MNRAS*, 515, 897
- Rodríguez, Ó., Pignata, G., Anderson, J. P., et al. 2020, *MNRAS*, 494, 5882

- Schroeder, K. P. 1985, *A&A*, 147, 103
- Shivvers, I., Modjaz, M., Zheng, W., et al. 2017, *PASP*, 129, 054201
- Singh, A., Kumar, B., Moriya, T. J., et al. 2019, *ApJ*, 882, 68
- Smartt, S. J. 2015, *PASA*, 32, e016
- Subrayan, B. M., Milisavljevic, D., Moriya, T. J., et al. 2022, arXiv e-prints, arXiv:2211.15702
- Sukhbold, T., Ertl, T., Woosley, S. E., Brown, J. M., & Janka, H. T. 2016, *ApJ*, 821, 38
- Tominaga, N., Blinnikov, S., Baklanov, P., et al. 2009, *ApJL*, 705, L10
- Tominaga, N., Morokuma, T., Blinnikov, S. I., et al. 2011, *ApJS*, 193, 20
- Tsuna, D., Murase, K., & Moriya, T. J. 2023, arXiv e-prints, arXiv:2301.10667
- Tsuna, D., Takei, Y., Kuriyama, N., & Shigeyama, T. 2021, *PASJ*, 73, 1128
- Ugliano, M., Janka, H.-T., Marek, A., & Arcones, A. 2012, *ApJ*, 757, 69
- Utrobin, V. P., & Chugai, N. N. 2013, *A&A*, 555, A145
- Yaron, O., Perley, D. A., Gal-Yam, A., et al. 2017, *Nature Physics*, 13, 510
- Yoon, S.-C., & Cantiello, M. 2010, *ApJL*, 717, L62



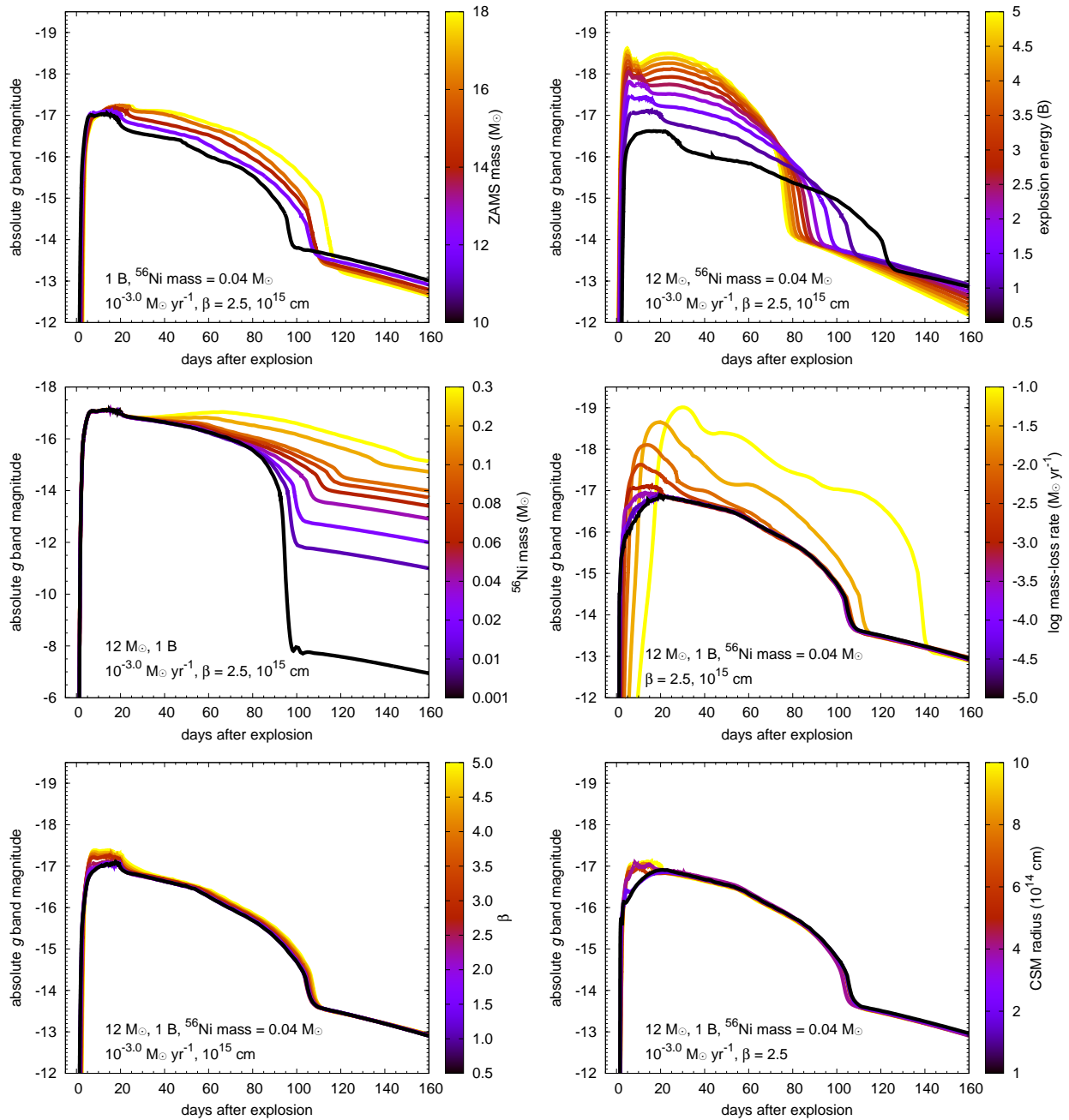


**Fig. 3.** Effects of each parameter on the LSST  $g$  band light curves. Each panel shows the effects of one parameter by only changing it. The other parameters are fixed in each panel.

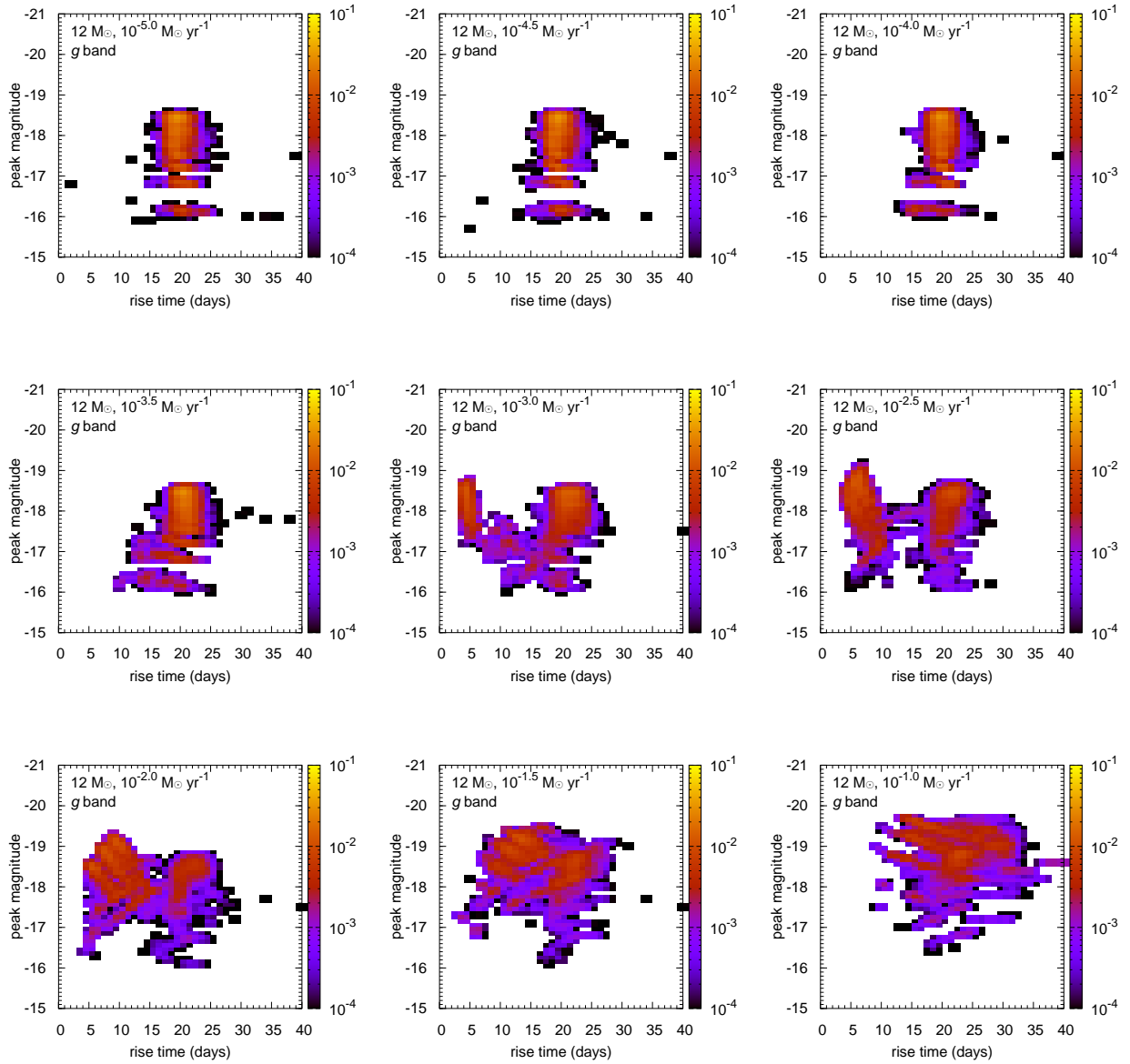


**Fig. 4.** Rise time and peak luminosity distributions of Type II SNe in the LSST *g* band from the  $12 M_{\odot}$  progenitor. The color contours show relative fractions of the models within each bin. Each panel shows a summary of all the models with one mass-loss rate.

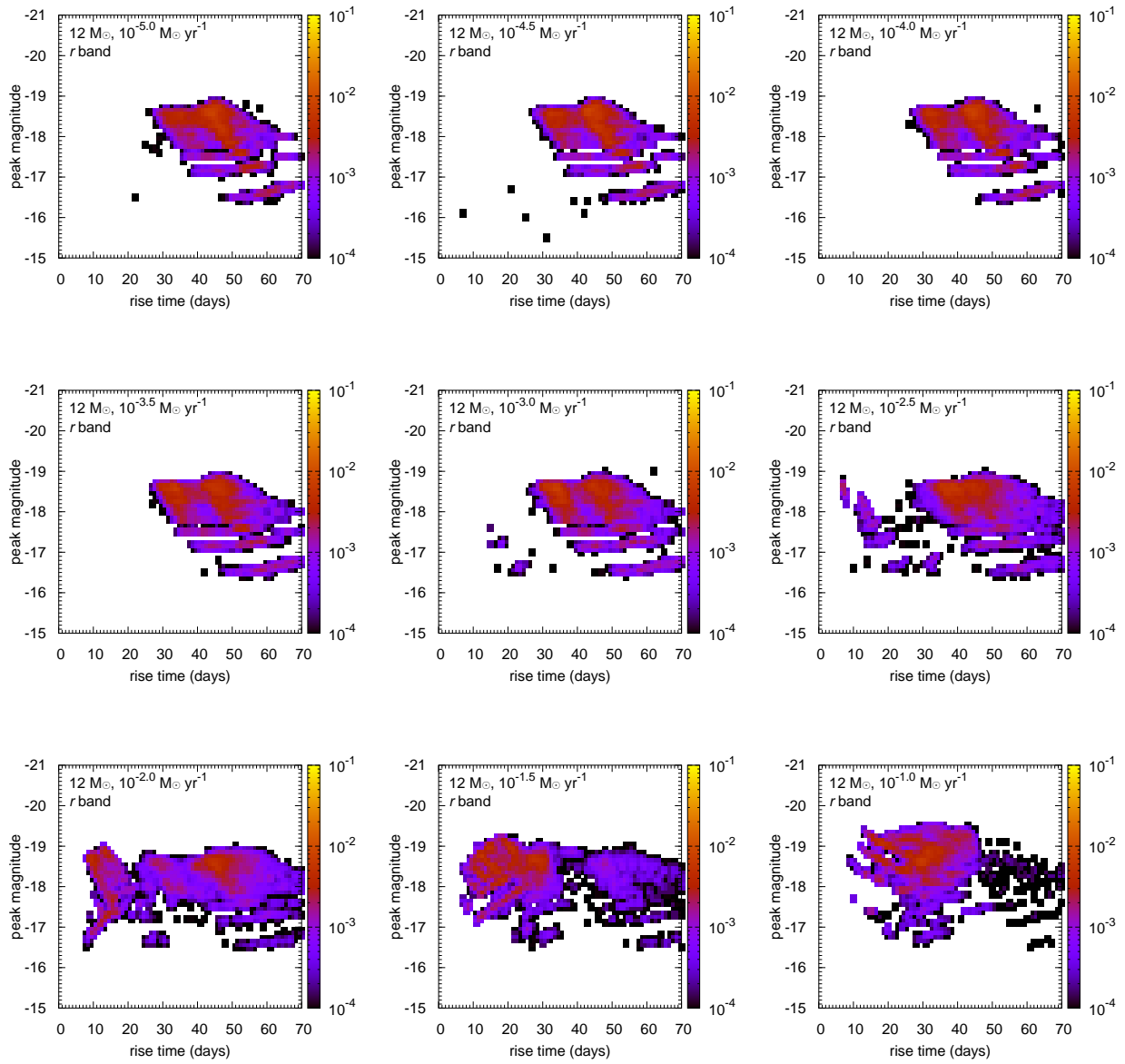
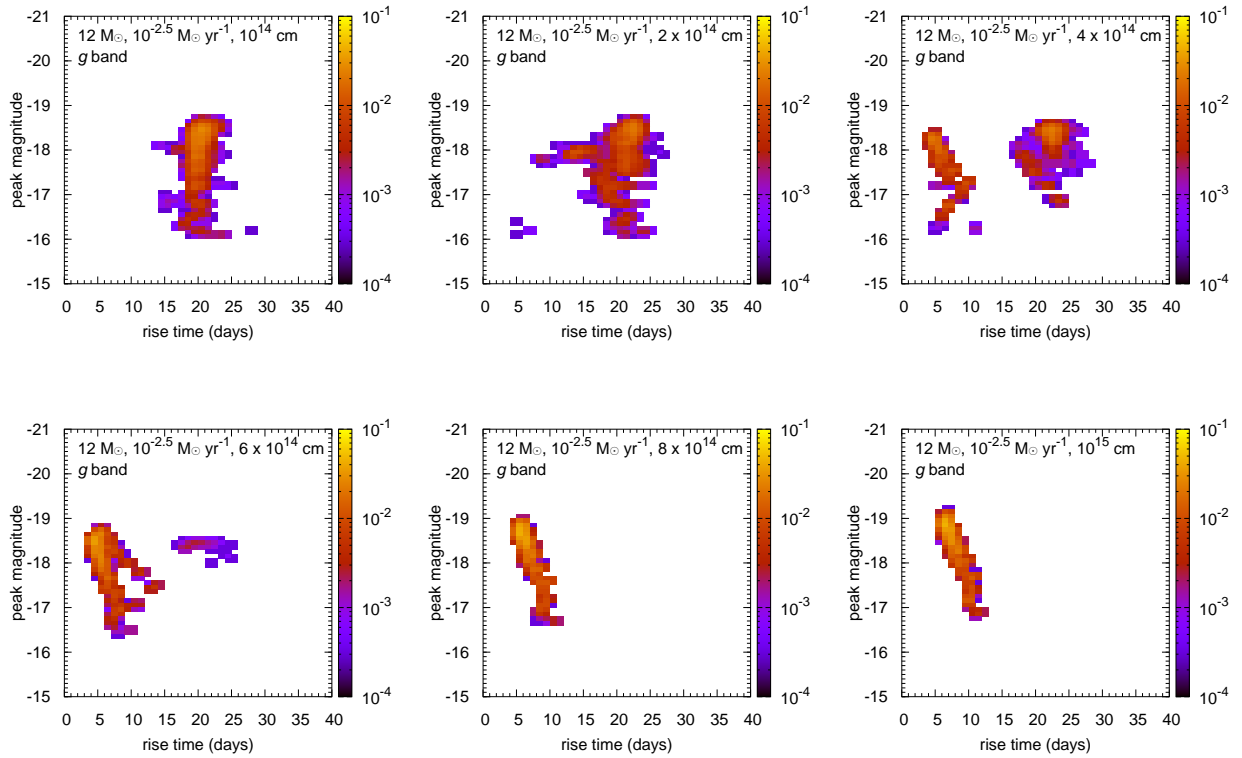
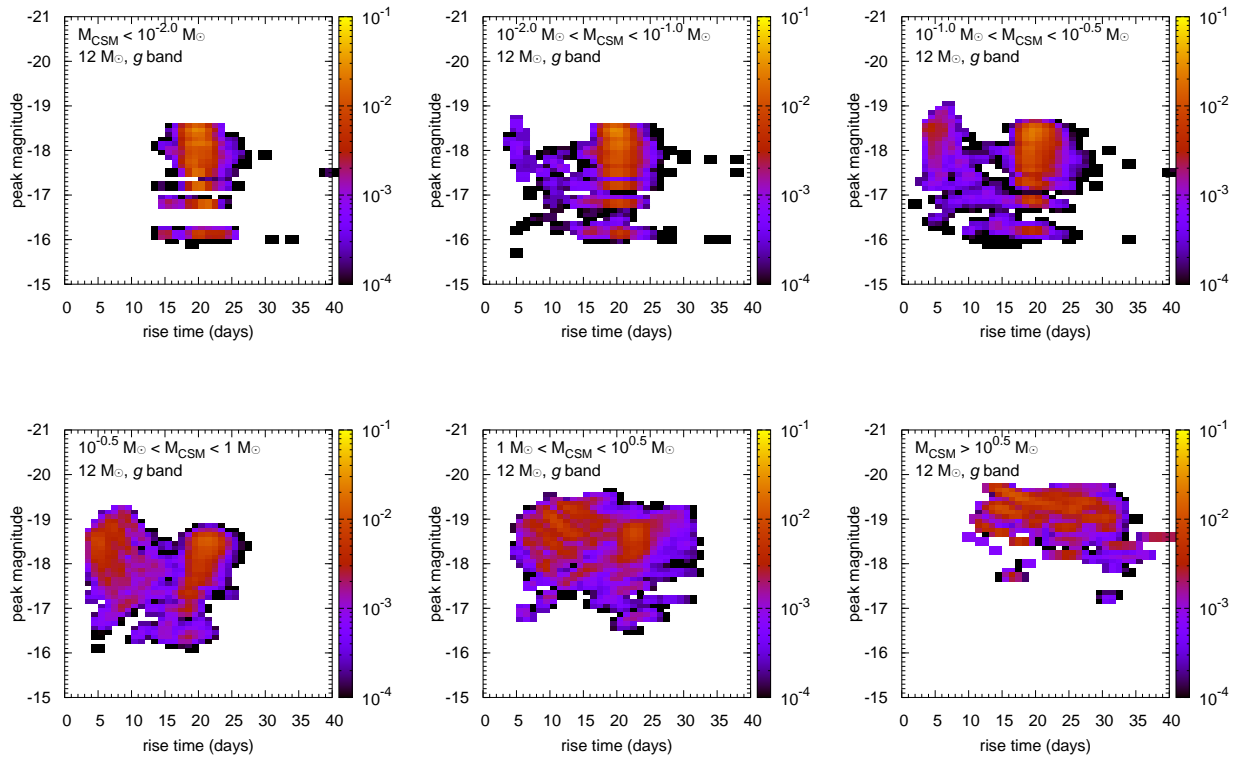


Fig. 5. Same as Fig. 4, but for the LSST *r* band filter.



**Fig. 6.** Rise time and peak luminosity distributions of Type II SNe from the  $12 M_{\odot}$  progenitor in the LSST *g* band with the same mass-loss rate ( $10^{-2.5} M_{\odot} \text{ yr}^{-1}$ ), but with different CSM radii. The color contours show relative fractions of the models within each bin. Each panel shows a summary of all the models with the CSM radius presented in the panel.



**Fig. 7.** Effects of CSM mass in the rise time and peak luminosity distributions of Type II SNe from the  $12 M_{\odot}$  progenitor in the LSST  $g$  band. The color contours show relative fractions of the models within each bin. Each panel shows a summary of all the models with the same CSM mass.

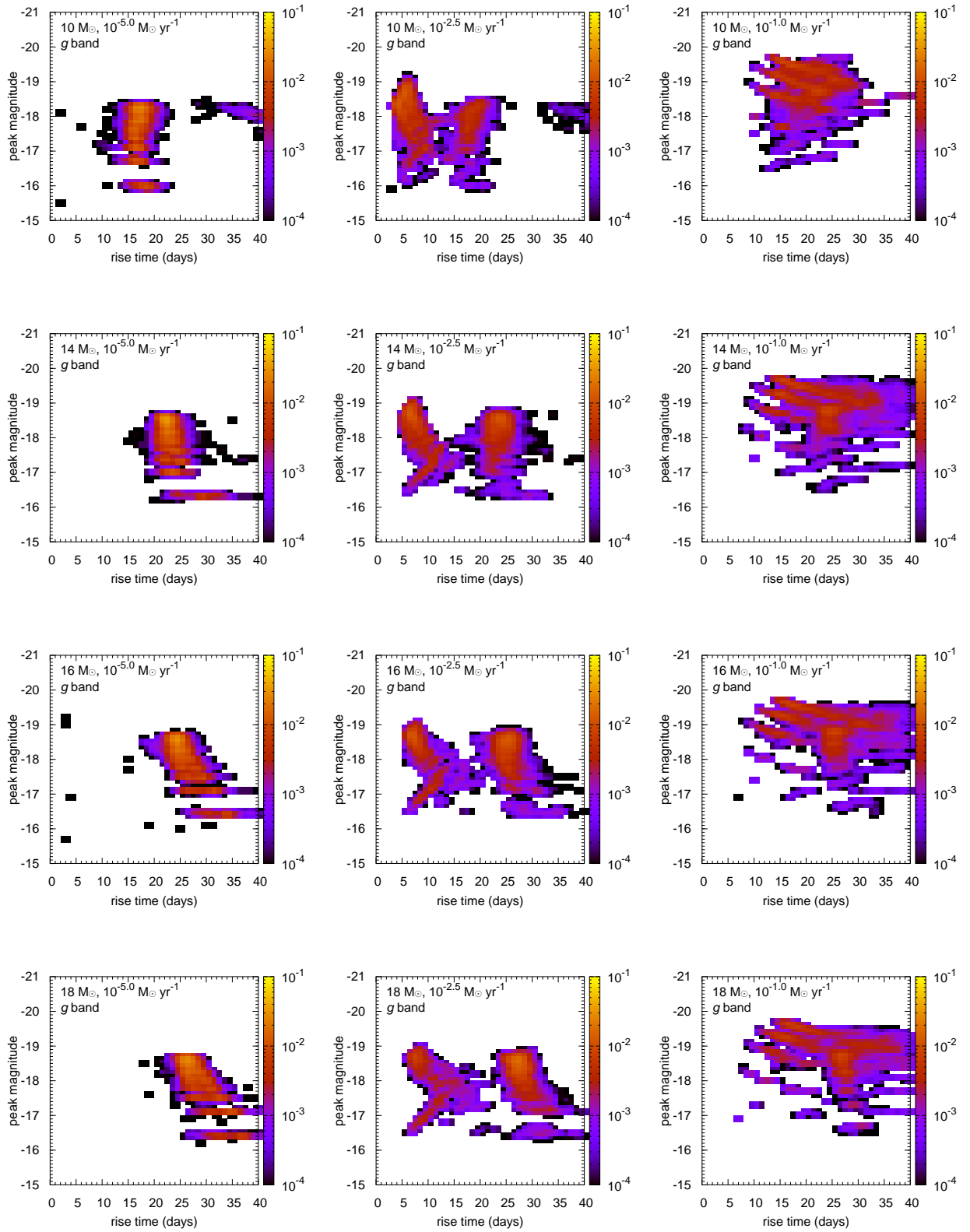


**Fig. 8.** Rise time and peak luminosity distributions of Type II SNe in the LSST *g* band from the 10, 14, 16, and 18  $M_{\odot}$  progenitors. The color contours show relative fractions of the models within each bin. Each panel shows a summary of all the models with one mass-loss rate.

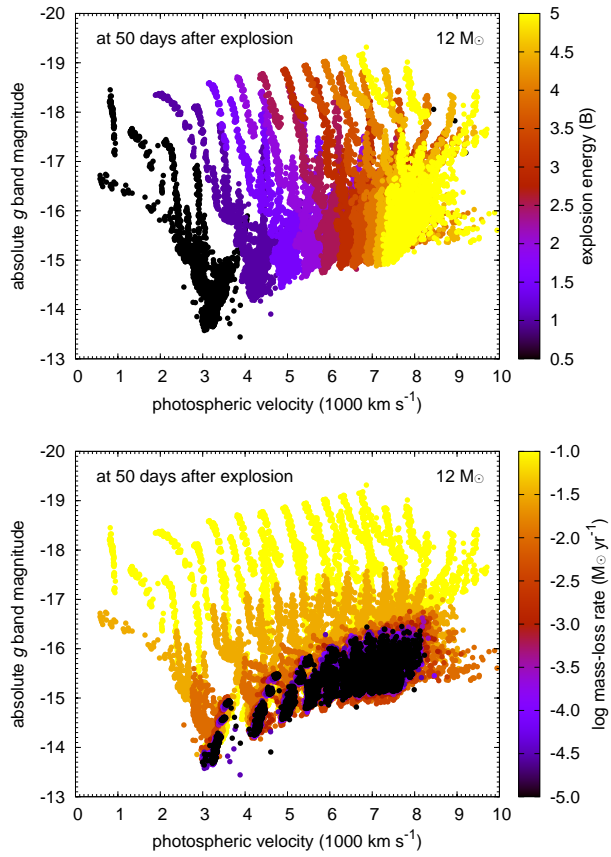


**Fig. 9.** Relation between photospheric velocity and LSST  $g$  band magnitude at 50 days after explosion in synthetic models with the  $12 M_{\odot}$  progenitor. The top panel presents the explosion energy of each model while the bottom panel shows the mass-loss rate of each model.

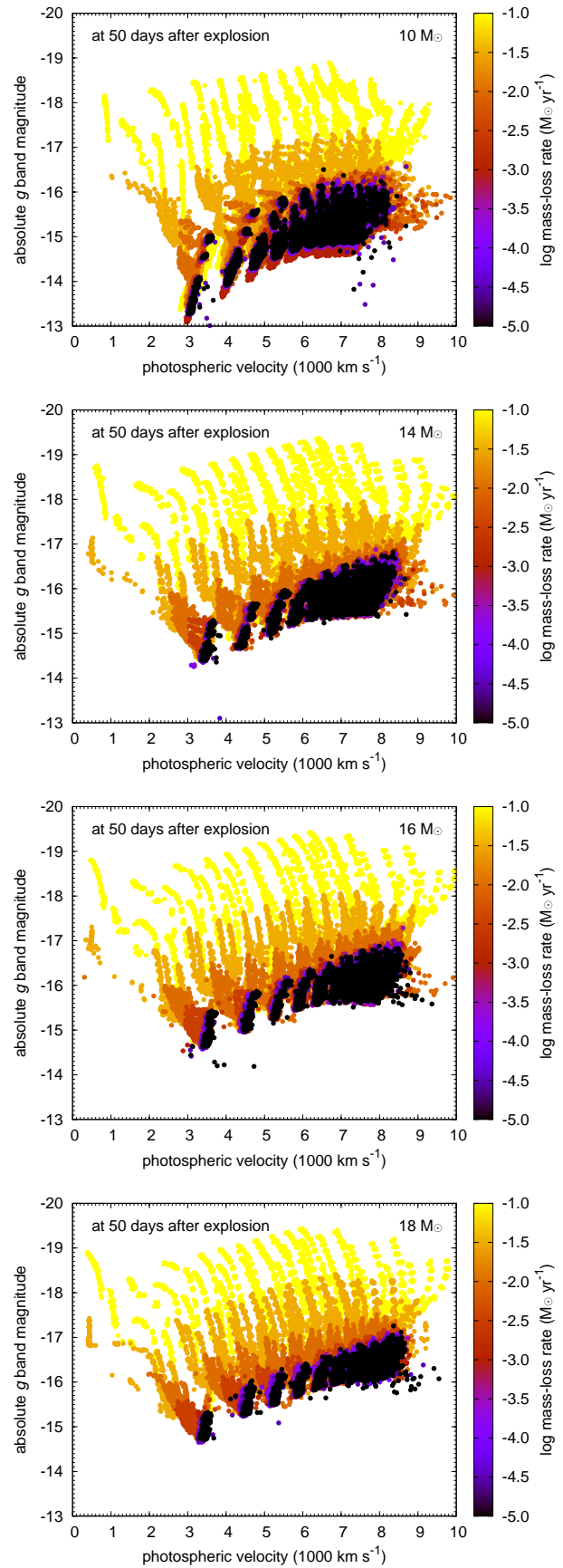


**Fig. 10.** Relation between photospheric velocity and LSST  $g$  band magnitude at 50 days after explosion in synthetic models with the  $10 M_{\odot}$ ,  $14 M_{\odot}$ ,  $16 M_{\odot}$ , and  $18 M_{\odot}$  progenitors. The mass-loss rate of each model is shown by color.